DOI: https://doi.org/10.15407/rpra30.02.077
UDC 621.396.962.

V.E. Kudryashov, K.A. Lukin, D.N. Tatyanko

O.Ya. Usikov Institute for Radiophysics and Electronics NAS of Ukraine
12, Acad. Proskury St., Kharkiv, 61085, Ukraine
E-mail: victor.e.kudryashov@gmail.com

NUMERICAL MODELING OF CHARACTERISTICS AND PARAMETERS OF A NOISE RADAR SENSOR FOR EARTH'S SURFACE MAPPING

Subject and Purpose. *The work presents numerical modeling results on the characteristics and parameters of a Noise Radar Sensor (NRS) during remote sensing of terrestrial surfaces. The radiometric (passive) mode and the mode with "backlighting" (active) of the mapping scene are considered. Radiometric signals of surfaces at wavelengths of 3.37 and 1.34 mm are used along with echo signals from the same surfaces under their backlighting (or illuminating) with ultra-weak-power quasi-continuous noise-like signals at a wavelength of 1.53 mm. The focus is on developing a numerical modeling technique to calculate the potential input characteristics of the NRS and compare them with the output parameters of the imagery.*

Methods and Methodology. *The obtained output parameters and characteristics of terrestrial surface imagery are analyzed and synthesized for potential NRS embodiments. The airborne NRS carrier is an AN-14 "Bdzhilka" aircraft. Attention is given to atmospheric conditions and limited time of accumulating useful low-contrast radiometric "grass–concrete" signals. Approximate effective specific grass and concrete scattering surfaces are sought under backlighting conditions.*

Results. *The numerical modeling results regarding the characteristics and parameters of the NRS embodiment have been optimized for two operating modes. The range, coverage sector of surfaces, imagery bands, resolution capability, number of Doppler filters at the NRS outputs, and accuracy features have been established in radiometric mode and during the backlighting of mapping surfaces.*

Conclusions. *Numerical modeling has been conducted based on technologically feasible characteristics of the NRS. The key parameters and features of the NRS in radiometric mode and under conditions of mapping scene backlighting have been optimized. We have analyzed the NRS input characteristics in connection with the output parameters of the imagery. The obtained results will allow us to predict the quality of imagery during remote sensing.*

Keywords: *radiometric contrast, grass, concrete, range, pixels, Doppler frequency correction, resolution, root mean square deviation of errors.*

1. Introduction. Statement of the Problem

The radiometric system resolution on the mapping surface is determined by the half-width of the antenna radiation pattern [1—5]. A bistatic radiometric system, like a Bistatic Radiometer (BR), circumvents this limitation by measuring the differences in the paths to the targets. Also, the BR structure allows determining the differential Doppler frequency correction for radio-brightness imagery [6, 7]. To enhance resolution by path difference, increase the range, and

Citation: Kudryashov, V.E., Lukin, K.A., Tatyanko, D.N., 2025. Numerical modeling of characteristics and parameters of a noise radar sensor for Earth's surface mapping. *Radio Phys. Radio Astron.*, **30**(2), pp. 77—88. https://doi.org/10.15407/rpra30.02.077

broaden the band of imagery, it makes sense to consider the Noise Radar Sensor (NRS) operation at wavelengths of 3 and 1 mm. Thus, the passive Earth's exploration system in [8] has a bandwidth of 6.0 GHz in the 3 mm range and 14.5 GHz in the 1 mm range. The useful signals are those from the mapping covers of grass and concrete. The NRS carrier can be an AN-14 "Bdzhilka" aircraft. The mapping surface image obtained under backlighting with ultra-weak-power broadband signals is correlated with the radiometric image. The joint processing of radiometric and backlighting images offers several advantages in the mapping plane interpretation [9], making the numerical modeling of NRS characteristics and parameters essential and informative for mapping various land covers.

The current literature [1, 3, 10, 11] does not provide data on the output characteristics and parameters of existing airborne NRS systems. There is little focus on the behavior of variables such as brightness range, imagery band, path difference resolution, and target velocities, which vary simultaneously [7, 10]. The publications do not provide numerical models, but rather general approaches to the issue. The technical implementation of backlighting for land covers does not enjoy attention either.

This work aims to develop a numerical modeling technique that gains the NRS characteristics and parameters for Earth's surface mapping based on the technical possibilities of radar constituents of the day.

2. Main Part

To implement the NRS system, its application conditions must be specified, and the NRS characteristics and parameters in the art must be understood. The NRS operation will be considered in the 3 mm and 1 mm wave ranges in the input bands as wide as 6.0 and 14.5 GHz, respectively [10]. The input bands determine the resolution on the mapping surface. The proper choice of the input bands reduces BR fluctuation sensitivity. One of the main technical characteristics is the range of the BR as part of the NRS. The condition of the radio-brightness temperature of atmospheric radiation can reduce the BR range.

1. Radio-brightness temperature in ambient conditions. The radio-brightness temperature $T_{at}(\varphi, A_{at}, R)$ of radiation from the atmospheric layer in between the mapping surface and the sensor at the zenith angle φ is determined by the formula [2, 12]

$$T_{at}(\varphi, A_{at}, R) \sim$$
$$\sim T_0 \left\langle 1 - \left\{ \exp\left[0.23 A_{at} R (\cos\varphi)^{-1} \right] \right\}^{-1} \right\rangle, \qquad (1)$$

where $T_0 = 290$ K is the absolute temperature near the Earth's surface, R is the range to the mapped object in kilometers (km), and A_{at} is the absorption coefficient (dB/km) of the radiometric signal in the presence of atmospheric oxygen, water vapor, and dust. We define the zenith angle φ to be 0°.

The flat mapping surface model with a horizontally homogeneous atmosphere is adopted. In clear weather, we restrict our consideration to the absorption by oxygen and water vapor (7.5 g/m^3). In rainy weather, the absorption coefficient A_{at} is sought in the medium rain, which is 4 mm/h in the 3 mm wave range and 5 mm/h in the 1 mm wave range. At the BR central wavelength $\lambda_1 = 3.37$ mm and $R = 5\,(2)$ km, expression (1) yields $T_{at}(0, 0.188, 5) \sim 56(24)$K in clear weather and $T_{at}(0, 2.89, 5) \sim 280(213)$K in the rain. When the BR central wavelength is $\lambda_2 = 1.34$ mm, with the ambient conditions unchanged, $T_{at}(0, 1.03, 5) \sim 201(109)$K in clear weather, and $T_{at}(0, 5.22, 5) \sim 289(264)$K in the rain.

2. Signal-to-noise ratio (SNR) at the BR output [7, 13, 14]. The coherent accumulation time $t(B_i)$, mathematical expectation $m_1(B_i)$ of a random process with its root mean square (RMS) deviation $\sigma_1(B_i)$ of errors, and the signal-to-noise ratio (SNR), denoted by $q_1(B_i)$ and consistent with bandpass B_i of the BR output RC filter, are calculated by the formulas

$$\begin{aligned} t(B_i) &= 3/B_i, \\ m_1(B_i) &= 1 - \exp\left[-B_i\, t(B_i) \right], \\ \sigma_1(B_i) &= \sqrt{1 - \exp\left[-2B_i\, t(B_i) \right]}, \\ q_1(B_i) &= m_1(B_i)/\sigma_1(B_i), \end{aligned} \qquad (2)$$

where B_i is the bandpass of the BR output filter. In our numerical modeling, B_i varies from 1 Hz to 1 kHz.

The mathematical expectation $m_2(B_i, B_e)$ of a random process and its RMS deviation $\sigma_2(B_i, B_e)$ of errors for the output RC Doppler filters, SNR values $q_2(B_i, B_e)$ at the outputs of the filters, and the SNR loss $A_{tt}(B_i, B_e)$ due to insufficient time for accumu-

lating useful signals come from the formulas

$$\begin{aligned} m_2(B_i,B_e) &= 1-\exp\left[-B_e\, t(B_i)\right], \\ \sigma_2(B_i,B_e) &= \sqrt{1-\exp\left[-2B_e\, t(B_i)\right]}, \\ q_2(B_i,B_e) &= m_2(B_i,B_e)\big/\sigma_2(B_i,B_e), \\ A_{tt}(B_i,B_e) &= \left[\, q_1(B_i)\big/q_2(B_i,B_e)\,\right]^2, \end{aligned} \tag{3}$$

where B_e is the bandpass of the BR output RC Doppler filter. In our modeling, B_e varies from 1 Hz to 1 kHz.

Provided that the differential Doppler frequency correction, F_p, for useful signals is measured, the SNR loss values are $A_{tt}(10^3,20) \sim 30.2$ or $A_{tt}(10^3,10) \sim 60.4$.

The SNR at the BR output with the coherent accumulation time fixed is

$$\nu(B_i,B_e) = \left[\nu_1 A_{tt}(B_i,B_e)\right]\big/\,0.9514, \tag{4}$$

where ν_1 is the SNR at which the probability of the correct object detection is $P = 0.5$, and the false alarm probability is $F = 10^{-1}$. Here, $\nu_1 = 2.32$ is chosen. The value 1/0.9514 derives from the fact that the accumulation time in the RC filters is limited and equals $3/B_i$.

The modeling results demonstrate that for B_i and B_e bands aligned, $\nu(10^3,10^3) \sim 2.44$. As a B_e decrease occurs while the differential Doppler frequency correction F_p is measured, the SNR increases considerably. Compare, e.g., $\nu(10^3,20) \sim 73.7$ and $\nu(10^3,10) \sim 147.3$. Then the F_p measurements of mapped objects require a BR range decrease. In this case, the SNR amounts 2.44 at the output of the Doppler filter with bandpass B_e.

3. Probability of correct object detection. The probability P of correct object detection at a fixed level of the false alarm probability F, the gains G_1, G_2, and G_3 of the NRS antennas, and the BR compression coefficients $K_{c1}(B_i)$ and $K_{c2}(B_i)$ in the 3 and 1 mm wave ranges are determined as [12, 15, 16]

$$\begin{aligned} P &= 1 - F^{(1+\nu_1)^{-1}}, \\ G_1 &= 3.2\cdot 10^4 D_1^2\left[\lambda_1\left(180/\pi\right)\right]^{-2}, \\ G_2 &= 3.2\cdot 10^4 D_1^2\left[\lambda_2\left(180/\pi\right)\right]^{-2}, \\ G_3 &= 3.2\cdot 10^4 D_1^2\left[\lambda_3\left(180/\pi\right)\right]^{-2}, \\ K_{c1}(B_i) &= 3B_{p1}B_i^{-1},\ K_{c2}(B_i) = 3B_pB_i^{-1}, \end{aligned} \tag{5}$$

where D_1 is the diameter of the NRS mirror antennas (here, $45\lambda_1 = 0.1517$ m), λ_3 (chosen to be 1.53 mm) is the central wavelength of the noise-like broadband signal for mapping surface backlighting, and B_{p1} and B_p are the BR transmission bandwidths of 6.0 and 14.5 GHz at λ_1 and λ_2, respectively.

4. Relation between useful signal power and BR channel noise. The relations $\gamma_1(B_i,B_e)$ and $\gamma_2(B_i,B_e)$ between useful signal average powers and intrinsic noises in the BR channels are [17, 18]

$$\begin{aligned} &\gamma_1(B_i,B_e) = \\ &= \frac{\nu(B_i,B_e) + \sqrt{\nu(B_i,B_e)\left[K_{c1}(B_i) - \nu(B_i,B_e)\right]}}{K_{c1}(B_i) - 2\nu(B_i,B_e)}, \\ &\gamma_2(B_i,B_e) = \\ &= \frac{\nu(B_i,B_e) + \sqrt{\nu(B_i,B_e)\left[K_{c2}(B_i) - \nu(B_i,B_e)\right]}}{K_{c2}(B_i) - 2\nu(B_i,B_e)}. \end{aligned} \tag{6}$$

5. BR range in Earth's surface mapping. The BR ranges $R_1(S,T,B_i,B_e)$ and $R_2(S,T,B_i,B_e)$ in the Earth's surface mapping at wavelengths λ_1 and λ_2, respectively, are calculated by the formulas [2, 19, 20]

$$\begin{aligned} &R_1(S,T,B_i,B_e) = \\ &= \sqrt{\frac{(1-\beta)\left|T - \left[\, t_{g1}C_1 + T_{at}(0,A_{at1},R)\,\right]\right| SG_1}{4\pi\alpha\gamma_1(B_i,B_e)L\left[T_0(K_1-\eta)+M_1\right]}}, \\ &R_2(S,T,B_i,B_e) = \\ &= \sqrt{\frac{(1-\beta)\left|T - \left[\, t_{g2}C_2 + T_{at}(0,A_{at2},R)\,\right]\right| SG_2}{4\pi\alpha\gamma_2(B_i,B_e)L\left[T_0\left(K_2-\eta\right)+M_2\right]}}, \\ &C_1 = \exp(-0.23A_{at1}R),\ C_2 = \exp(-0.23A_{at2}R), \end{aligned} \tag{7}$$

where S is the mapped object area varying from 1 to $4\cdot 10^2$ m^2 and T is the object radio-brightness temperature varying from 160 to 320 K. Ibidem, β is the coefficient that takes into account signals from outside the main lobe of the antenna radiation pattern ($\beta = 0.31$), t_{g1} (295 K) and t_{g2} (292 K) are the radio-brightness temperatures of the mapped surface (grass) at radiation wavelengths λ_1 and λ_2, respectively [1], A_{at1} and A_{at2} are the coefficients of the radiometric signal absorption by oxygen and water vapor present in the atmosphere (in clear weather, $A_{at1} \sim 0.188$ dB/km at λ_1 and $A_{at2} \sim 1.03$ dB at λ_2), R is the range to the mapped object ($R = 2$ km), α is the BR constant and L is the NRS sensor loss ($\alpha = \sqrt{2}$, $L = 2$), $K_1 = 3.36$ and $K_2 = 6.67$ are the noise figures of the BR channels [17], and η is the efficiency

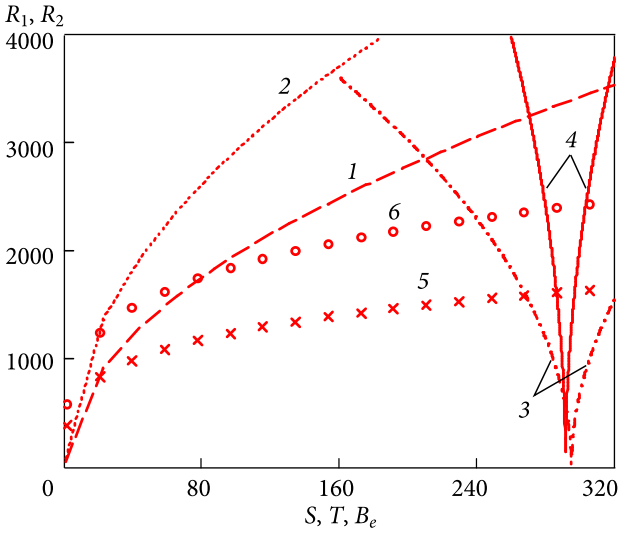

Fig. 1. The calculated BR ranges R_1 (S, T, B_i, B_e) (curves *1*, *3*, *5*) and R_2 (S, T, B_i, B_e) (curves *2*, *4*, *6*)

of the BR antennas ($\eta = 0.78$). Additionally,

$$M_1 = \eta\left[T_{at}(\varphi, A_{at1}, R) + t_{g1}C_1 + \right.$$
$$\left. +(1-\beta)\sum_{i=1}^{n} t_i C_1 \delta_i + \beta\sum_{j=1}^{k} t_j C_1 \delta_j \right],$$
$$M_2 = \eta\left[T_{at}(\varphi, A_{at2}, R) + t_{g2}C_2 + \right. \quad (8)$$
$$\left. +(1-\beta)\sum_{i=1}^{n} t_i C_2 \delta_i + \beta\sum_{j=}^{k} t_j C_2 \delta_j \right],$$

where $T_{at}(\varphi, A_{at1}, R)$ and $T_{at}(\varphi, A_{at2}, R)$ are the radio-brightness radiation temperatures of the atmospheric layer in between the surface and the NRS sensor at wavelengths λ_1 and λ_2, respectively (see expression (1)), t_i and t_j with $i = 1, 2, \ldots n$ and $j = 1, 2, \ldots k$ are the radio-brightness temperatures of mapping surface interferences in, respectively, the main and side lobes of the BR antennas, and δ_i and δ_j are the solid angles of the mapped objects in the main and side lobes of the BR antennas.

If the mapped object is such that $\delta_i = 20\%$ and the weather is clear, then $M_1 \sim 324.3$ K at λ_1. For λ_2 and $\delta_i = 50\%$ with the weather clear, we have $M_2 \sim 320.1$ K.

Theoretical and experimental studies [1] are available for various land covers and horizontal polarization, with a 40° reception angle, and wavelengths of 2.15 and 8 mm [1]. The conducted large-scale modeling yields approximate radio-brightness temperatures of certain land covers and "grass–concrete" contrasts [15] in the form

$$\Delta_{3.37} = \Delta_{2.15}\sqrt{\lambda_1/\lambda_{2.15}},$$
$$\Delta_{1.34} = \Delta_{2.15}\sqrt{\lambda_2/\lambda_{2.15}}, \quad (9)$$

where $\Delta_{3.37}, \Delta_{1.34}$ are the radio-brightness "grass–concrete" contrasts at λ_1 and λ_2, respectively, and $\Delta_{2.15}$ is the "grass–concrete" contrast at $\lambda_{2.15} = 2.15$ mm.

We obtained $\Delta_{3.37} \sim 44$ K and $\Delta_{1.34} \sim 28$ K, $T_{concrete1} \sim 251$ K at λ_1 and $T_{concrete2} \sim 264$ K at λ_2.

Curves *1*, *3*, and *5* in Fig. 1 plot for $\lambda_1 = 3.37$ mm the calculated BR ground mapping ranges $R_1(S, 254, 10^3, 10^3)$, $R_1(10^2, T, 10^3, 10^3)$, and $R_1(10^2, 254, 10^3, B_e)$, respectively. Curves *2*, *4*, and *6* plot $R_2(S, 274, 10^3, 10^3)$, $R_2(10^2, T, 10^3, 10^3)$, and $R_2(10^2, 274, 10^3, B_e)$, respectively, for $\lambda_2 = 1.34$ mm. For curves *3* and *4*, the smallest operating range values correspond to the ultra-low contrasts on the mapping surface. Thus, $R_{1ij} = 0$ when $T \sim 294.6$ K (curve *3*), and $R_{2ij} = 0$ when $T \sim 291.2$ K (curve *4*).

The range $R_1(10^2, 254, 10^3, 10^3) \sim 1984$ m corresponds to λ_1 with "grass–concrete" contrast ~40 K. Also, $R_1(10^2, 254, 10^3, 20) \sim 848$ m is for the Doppler frequency correction F_p measured. At λ_2 and "grass–concrete" contrast ~ 17 K, we have $R_2(10^2, 274, 10^3, 10^3) \sim$ ~ 2949 m and $R_2(10^2, 274, 10^3, 20) \sim 1258$ m with the F_p correction measured.

We note that the BR operating range in the 1 mm wavelength band is longer by a factor of about 1.49 than the BR range in the 3 mm band. Further, we restrict ourselves to the BR modeling at $\lambda_2 = 1.34$ mm alone.

6. The reception radius of Earth's surface signals. The radius $r_2(S, T, B_i, B_e)$ of signal reception from Earth's surface, the reception area $S_2(S, T, B_i, B_e)$, and the solid angle $\Omega(S, T, B_i, B_e)$ of the mapped object on the mapping surface in per cent are [18]

$$r_2(S, T, B_i, B_e) =$$
$$= R_2(S, T, B_i, B_e)\sin\left[\left(\sqrt{2}\pi\Theta_2\right)/360\right],$$
$$S_2(S, T, B_i, B_e) = \pi r_2(S, T, B_i, B_e)^2, \quad (10)$$
$$\Omega(S, T, B_i, B_e) = 10^2 S\left[\pi r_2(S, T, B_i, B_e)^2\right]^{-1},$$

where the first expression gives the image surface radius if it aligns the normal to the BR base.

For example, we obtained $r_2(10^2, 274, 10^3, 20) \sim 7.9$ m, $S_2(10^2, 274, 10^3, 20) \sim 194$ m^2, and $\Omega(10^2, 274, 10^3, 20) \sim$ $\sim 51.6\%$

7. BR resolution on Earth's surface. The equation of a hyperboloid of revolution yields the BR resolution $P_r(n_d, S, T, B_i, B_e)$ on Earth's surface and the number of path difference intersections (hyperbolas) in a single pixel of the radiometric image across a half-width of the signal cross-correlation function $K_x(n_d, S, T, B_i, B_e)$ [19, 21] as follows

$$P_r(n_d, S, T, B_i, B_e) = \sqrt{\left\{1 - \frac{R_2(S, T, B_i, B_e)}{\left[(2n_d c)/B_2\right]^2 - (B/2)^2}\right\}\left(\frac{n_d c}{B_2}\right)^2},$$
$$K_x(n_d, S, T, B_i, B_e) = \left\{\left[4r_2(S, T, B_i, B_e)\right]/P_r(S, T, B_i, B_e)\right\}, \quad (11)$$

where n_d is the tap number of the BR delay line, c is the speed of light $(3 \cdot 10^8$ m/s), and B is the distance between the BR reception points (the BR base).

The modeling results are $P_r(1, 10^2, 274, 10^3, 10^3) \sim$ ~ 12.2 m, $P_r(1, 10^2, 274, 10^3, 20) \sim 5.2$ m, and $K_x(1, 10^2, 274, 10^3, 10^3) = K_x(1, 10^2, 274, 10^3, 20) \sim 6.04$ m.

8. Fulfilment of mapping continuity. To ensure continuity in the mapping, the first line of the image can be constructed utilizing the widths of the BR antenna patterns. The second line uses the half-widths of the antenna patterns and is shifted by the radius of the "spot" on the mapping surface. The time $t_p(S, T, B_i, B_e)$ taken to construct one line of the image, the number $n_k(S, T, B_i, B_e)$ of steps in one line, and the radiometric image band $B_{im}(S, T, B_i, B_e)$ are determined by the formulas [18]

$$t_p(S, T, B_i, B_e) = r_2(S, T, B_i, B_e)/\vec{V}_c,$$
$$n_k(S, T, B_i, B_e) = t_p(S, T, B_i, B_e)/t_p(B_i),$$
$$B_{im}(S, T, B_i, B_e) = \left[2r_2(S, T, B_i, B_e)^2\right]/\left[\vec{V}_c\, t_p(B_i)\right], \quad (12)$$

where $\vec{V}_c$ is the AN-14 flight velocity (50 m/s) during the Earth's surface mapping.

The calculation results by expression (12) are viewed in Fig. 2. The dependences $R_2(10^2, T, 10^3, 10^3)$ and $B_{im}(10^2, T, 10^3, 10^3)$ (curves *1* and *2*, respectively) illustrate a relative growth of the image band at high contrasts of the useful signals. To avoid merging with curves *1* and *2*, dependences $R_2(10^2, T+50, 10^3, 20)$

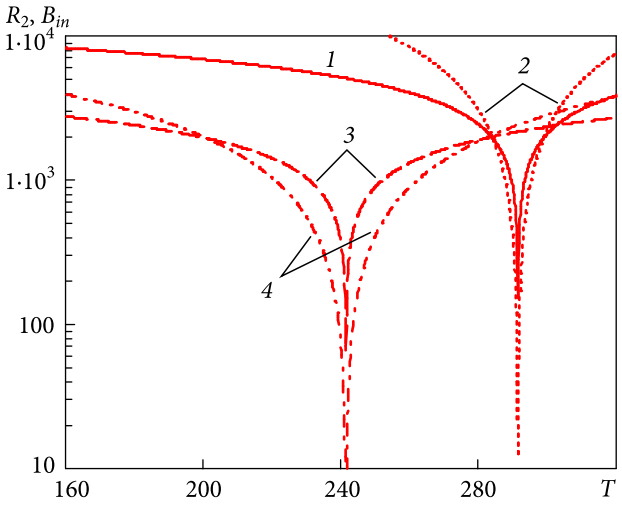

Fig. 2. The range $R_2(S, T, B_i, B_e)$ of the BR as part of the NRS and the land surface mapping band $B_{im}(S, T, B_i, B_e)$ versus the object radio-brightness temperature T

and $B_{im}(10^2, T+50, 10^3, 20)$ (curves *3* and *4*, respectively) are temperature-shifted by 50 K. The measurement of the Doppler frequency correction F_p significantly reduces the BR range and the mapping band.

We obtained $B_{im}(10^2, 274, 10^3, 10^3) \sim 4528$ m when $R_2(10^2, 274, 10^3, 20) \sim 2949$ m. And in the F_p presence, $B_{im}(10^2, 274, 10^3, 20) \sim 823$ m and $R_2(10^2, 274, 10^3, 20) \sim 1258$ m. Hence, the F_p measurement for the BR reduces the radiometric image band by ~ 5.5 times with a loss of range by ~ 2.3 times.

9. Optimal relation between BR range and image band. Viewing angles of BR antennas. The calculation formulas for the $N(B_i, k)$ relation between the BR range and the image band and for the antenna viewing angle $\Omega(B_i, k)$ are given below

$$N(B_i, k) = \frac{R_2\left(10^2, 264, B_i, \frac{B_i}{k}\right)}{B_{im}\left(10^2, 264, B_i, \frac{B_i}{k}\right)},$$
$$\Theta(B_i, k) = a\sin\left\{\frac{0.5B_{im}\left(10^2, 264, B_i, \frac{B_i}{k}\right)}{R_2\left(10^2, 264, B_i, \frac{B_i}{k}\right)}\right\}\frac{180}{\pi}, \quad (13)$$

where the k-times decreased bandpass B_i of the BR output filter stands instead of the bandpass B_e of the Doppler filter.

We obtained $N(10^3, 1) \sim 0.65$ and $\Theta(10^3, 1) \sim$ $\sim 50.1°$, which are extremely difficult to imple-

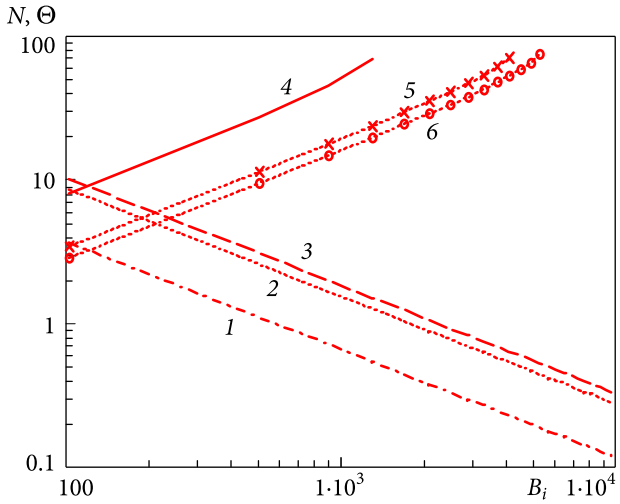

Fig. 3. The relation $N(B_i, k)$ between the BR range and the image band. The viewing angles $\Theta(B_i, k)$ of BR antennas versus output filter bandpass B_i

ment aboard an aircraft AN-14 "Bdzhilka". With F_p measured, $N(10^3,50) \sim 1.53$ and $\Theta(10^3,50) \sim$ $\sim 19.1°$. These numerical modeling results plotted in Fig. 3 serve to optimize the BR characteristics and parameters. The mapping according to $N(B_i, 1)$ (curve *1*) and $\Omega(B_i,1)$ (curve *4*) suggests choosing $B_i \sim 589$ Hz when $\Theta(589,1) \sim 31°$. In this case, $N(589,1) \sim 1$, $R_2(10^2,274,589,589) \sim 3367$ m, and $B_{im}(10^2,274,589,589) \sim 3475$ m. Similarly, the dependences $N(B_i,50)$ (line *2*) and $\Omega(B_i,50)$ (curve *5*) taking into account the F_p measurements are also shown. We obtained $N(1835,50) \sim 1$, $\Theta(1835,37) \sim 31°$, $R_2(10^2,274,1835,37) \sim 1083$ m, and $B_{im}(10^2,274,1835,37) \sim 1119$ m. A hundredfold narrowing of the B_i is given by the dependences $N(B_i,10^2)$ (line *3*) and $\Theta(B_i,10^2)$ (curve *6*). As before, $N(2313,10^2) \sim 1$, $\Theta(2313,10^2) \sim 31°$, $R_2(10^2,274,2313,23) \sim 886$ m, and $B_{im}(10^2,274,2313,23) \sim 882$ m.

Optimization is generally possible according to one of the following values, including useful-signal radio-brightness contrasts on the mapping surface, BR operating range, image band, differential Doppler frequency, viewing angles, etc.

10. Differential Doppler frequency correction $F_p(\vec{V}_o,\eta,S,T,B_i,B_e)$ of objects on the mapping surface [19, 20]. Figure 4 shows the two, B_1 and B_2 reception points of the BR. The distance between B_1 and B_2 is called the base B. The vectors $\vec{V}_c$ and $\vec{V}_o$ are, respectively, the carrier flight velocity and the object movement velocity (the ground surface wind velocity). The object is at the point 0 and represents a piece of concrete at $T = 264$ K surrounded by some grass at $T = 292$ K. The carrier flight direction is given by segment AO. In our numerical modeling, $B =$ $= 10$ m, $\vec{V}_c = 50$ m/s, and $\vec{V}_o$ varies within 0 to 30 m/s. The differential Doppler frequencies of objects will be calculated by the formulas derived below.

The length $OB_3(S,T,B_i,B_e)$ of the image line (in Fig. 4, line OB_3) and the angle $\alpha(S,T,B_i,B_e)$ (in Fig. 4, angle B_2OB_3) are

$$\begin{aligned} &OB_3(S,T,B_i,B_e) = \\ &= B_{im}(S,T,B_i,B_e) - 0.5\left[B_{im}(S,T,B_i,B_e) - B\right], \\ &\alpha(S,T,B_i,B_e) = \\ &= a\cos\left[OB_3(S,T,B_i,B_e)/R_2(S,T,B_i,B_e)\right]. \end{aligned} \tag{14}$$

The carrier flight altitude $B_2B_3(S,T,B_i,B_e)$ (straight line B_2B_3) and the range $OB_1(S,T,B_i,B_e)$ from the receiving point B_1 to the object (straight line OB_1) are

$$\begin{aligned} &B_2B_3(S,T,B_i,B_e) = \\ &= \sqrt{R_2(S,T,B_i,B_e)^2 + OB_3(S,T,B_i,B_e)^2}, \\ &OB_1(S,T,B_i,B_e) = \\ &= \sqrt{B_2B_3(S,T,B_i,B_e)^2 + 0.5[B_{im}(S,T,B_i,B_e) - B]^2}. \end{aligned} \tag{15}$$

The angle $\beta(S,T,B_i,B_e)$ (angle B_1OB_3) and the angle $\gamma(S,T,B_i,B_e)$ (angle B_1OB_2) are

$$\begin{aligned} &\beta(S,T,B_i,B_e) = \\ &= a\cos\left\{\frac{0.5\left[B_{im}(S,T,B_i,B_e) - B\right]}{OB_1(S,T,B_i,B_e)}\right\}, \\ &\gamma(S,T,B_i,B_e) = \beta(S,T,B_i,B_e) - \alpha(S,T,B_i,B_e). \end{aligned} \tag{16}$$

The dynamic velocity $\vec{V}_d(\vec{V}_o,\mu)$ (vector $\vec{V}_d$) of the mapped object and the angle $\theta(\vec{V}_o,\mu)$ (angle θ) between the $\vec{V}_c$ and $\vec{V}_d$ are

$$\begin{aligned} &\vec{V}_d(\vec{V}_o,\mu) = \sqrt{\vec{V}_o^2 + \vec{V}_c^2 - 2\vec{V}_o\vec{V}_c\cos(\pi - \mu)}, \\ &\theta(\vec{V}_o,\mu) = a\cos\left\{\frac{\vec{V}_c^2 + \vec{V}_d(\vec{V}_o,\mu)^2 - \vec{V}_o}{2\vec{V}_c\,\vec{V}_d(\vec{V}_o,\mu)}\right\}. \end{aligned} \tag{17}$$

Here the angle μ between $\vec{V}_c$ and $\vec{V}_o$ varies in our modeling from 0.0175 to 2.5 π.

The projection $\vec{V}_p(\vec{V}_o,\mu)$ (vector $\vec{V}_p$) of the object dynamic velocity onto the mapping plane and

the projections of the object movement velocities $\vec{V}_1(\vec{V}_o,\mu,S,T,B_i,B_e)$ (vector $\vec{V}_1$) and $\vec{V}_2(\vec{V}_o,\mu,S,T,B_i,B_e)$ (vector $\vec{V}_2$) in the directions to the reception points B_1 and B_2, respectively, are

$$\begin{aligned}
&\vec{V}_p(\vec{V}_o,\mu)=\vec{V}_d(\vec{V}_o,\mu)\cos\left[0{,}5\pi-\theta(\vec{V}_o,\mu)\right],\\
&\vec{V}_1(\vec{V}_o,\mu,S,T,B_i,B_e)=\\
&=\vec{V}_p(\vec{V}_o,\mu)\cos\left[\beta(\vec{V}_o,\mu,S,T,B_i,B_e)\right],\\
&\vec{V}_2(\vec{V}_o,\mu,S,T,B_i,B_e)=\\
&=\vec{V}_p(\vec{V}_o,\mu)\cos\left[\alpha(\vec{V}_o,\mu,S,T,B_i,B_e)\right].
\end{aligned}\qquad(18)$$

The differential Doppler frequency correction $F_p(\vec{V}_o,\mu,S,T,B_i,B_e)$ of objects on the mapping surface is [19, 20]

$$\begin{aligned}
F_p(\vec{V}_o,\mu,S,T,B_i,B_e)&=\frac{-2\vec{V}_p(\vec{V}_o,\mu)}{\lambda_2}\times\\
\times\sin&\left[\frac{\beta(\vec{V}_o,\mu,S,T,B_i,B_e)+\alpha(\vec{V}_o,\mu,S,T,B_i,B_e)}{2}\right]\times\\
\times\sin&\left(\frac{\gamma(\vec{V}_o,\mu,S,T,B_i,B_e)}{2}\right).
\end{aligned}\qquad(19)$$

The $F_p(\vec{V}_o,\mu,S,T,B_i,B_e)$ calculation results are shown in Fig. 5. The dependences $F_p(\vec{V}_o,1,10^2,274,10^3,20)$ (straight line *1*) and $F_p(5,\mu,10^2,274,10^3,20)$ (curve *2*) describe, correspondingly, the differential frequency F_{pij} growth as the object velocity $\vec{V}_o$ increases and the angle μ between the carrier speed $\vec{V}_c$ and the object speed $\vec{V}_o$ changes.

If $\mu=\pi$ or 2π, then $F_{pij}=0$, since $\vec{V}_{1ij}=\vec{V}_{2ij}=0$ (see (19)). The dependences $F_p(5,1,S,274,10^3,20)$ (straight line *3*) and $F_p(5,1,10^2,T,10^3,20)$ (curve *4*) describe the F_{pij} behavior depending, respectively, on areas S of the objects and their radio-brightness temperatures T. The steep F_{pij} rise along curve *4* is associated with a low radio-brightness contrast wherein the BR range R_{2ij} significantly decreases and the angle γ_{ij} from formula (16) increases. When $R_2(10^2,274,10^3,10^3)\sim 2949$ m and $B_{im}(10^2,274,10^3,10^3)\sim 4528$ m, the highest differential frequency value is as low as $F_p(30,1,10^2,274,10^3,10^3)\sim 26.2$ Hz. That is, at $\vec{V}_o=30$ m/s and $B_e=10^3$ Hz, the differential frequency is not measured. The Doppler filter bandpass B_e narrowing from 1 kHz to 20(10) Hz gives $R_2(10^2,274,10^3,20)\sim$ ~ 1258 (1057)m, $B_{im}(10^2,274,10^3,20)\sim 823$ (582)m,

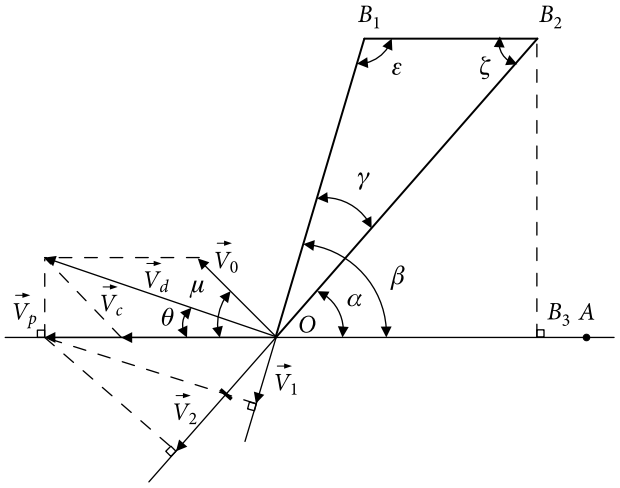

Fig. 4. Determination of the differential Doppler frequency of mapped objects.

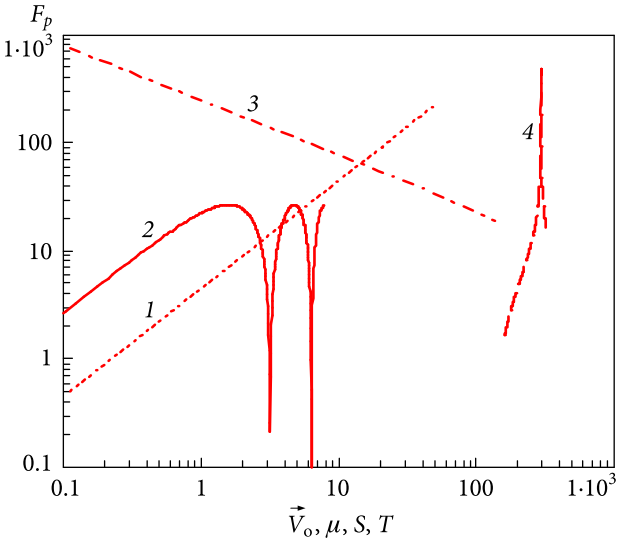

Fig. 5. Differential Doppler frequency correction $F_p(\vec{V}_o,\mu,S,T,B_i,B_e)$ of objects on the mapping surface versus variables $\vec{V}_o,\mu,S$, and T: *1* — $F_p(\vec{V}_o,1,10^2,274,10^3,20)$; *2* — $F_p(5,\mu,10^2,274,10^3,20)$; *3* — $F_p(5,1,S,274,10^3,20)$; *4* — $F_p(5,1,10^2,T,10^3,20)$

$F_p(4.5,1,10^2,274,10^3,20)\sim 20.1$ Hz, and $F_p(1.9,1,10^2,274,10^3,10)\sim 10.4$ Hz. We note that measuring the object velocity $\vec{V}_o=4.5$ (1.9) m/s can be accompanied by losses in the BR range and radiometric image band.

11. Number of Doppler filters at the BR output and coverage sector of BR antennas. The number $N_f(\vec{V}_o,\mu,S,T,B_i,B_e)$ of necessary Doppler filters at the BR output and the coverage sector $\theta_s(S,T,B_i,B_e)$ of the BR antenna system are given by the

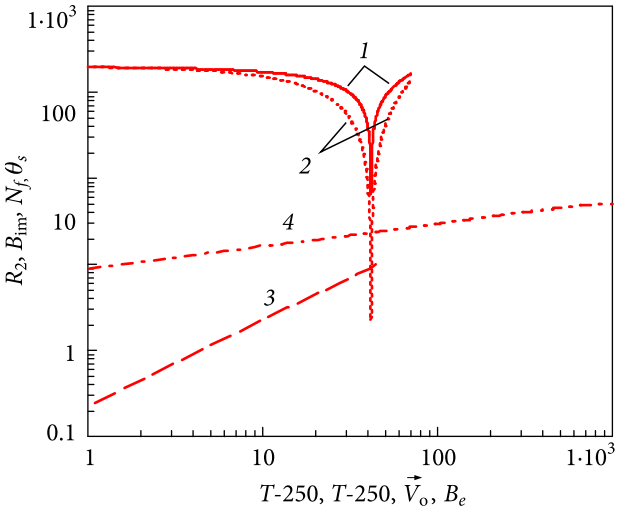

Fig. 6. BR range $R_2(S,T,B_i,B_e)$, image band $B_{im}(S,T,B_i,B_e)$, filter number $N_f(\vec{V}_o,\mu,S,T,B_i,B_e)$ at the BR output, and coverage sector $\theta_2(S,T,B_i,B_e)$ of the BR antenna system as functions of T, $\vec{V}_0$, and B_e variables

formulas [18]

$$N_f(\vec{V}_o,\mu,S,T,B_i,B_e)=F_p(\vec{V}_o,\mu,S,T,B_i,B_e)\big/B_e,$$
$$\theta_s(S,T,B_i,B_e)=a\sin\left[\frac{0.5B_{im}(S,T,B_i,B_e)}{R_2(S,T,B_i,B_e)}\right]\frac{180^o}{\pi}. \quad (20)$$

The BR calculation results with F_{pij} measured are seen in Fig. 6. The dependences $R_2(10^2,T,10^3,20)$ and $B_{im}(10^2,T,10^3,20)$ (curves 1 and 2, respectively) show the BR range and the image band implemented. For clarity, the curves are mutually shifted by 250 K. Straight lines *3* and *4* illustrate, respectively, the number $N_f(\vec{V}_o,1,10^2,274,10^3,20)$ of the necessary Doppler filters and the coverage sector $\theta_s(10^2,274,10^3,B_e)$ of the BR antenna system. According to curve *4* without F_{pij} ($B_i=B_e=10^3$ Hz) measuring, the antenna system should have ±50.1° coverage sector, which is technically difficult to implement. At the same time, at these probing angles, the radiative capacity of the land covers decreases, while the radio-brightness contrast between the corresponding surfaces increases.

We obtained $R_2(10^2,274,10^3,30)\sim 1392$ m, $B_{im}(10^2,274,10^3,30)\sim 1008$ m, $N_f(30,1,10^2,270,10^3,30)\sim 4$, $F_p(7.7,1,10^2,274,10^3,30)\sim 30.2$ Hz, and $\theta_s(10^2,274,10^3,30)\sim\pm 21.2°$.

12. Specific effective surfaces for concrete and grass. More information about various land covers is attained through mapping scene backlighting with a weak broadband noise-like signal [9, 20]. As a rule, the backlighting is carried out at a frequency closest to the central frequency of the BR operation under the Radio Regulations [8]. Then the NRS performs as a joint, angle-and-range-measuring radar system [15, 20]. The central frequency of backlighting with a noise-like signal was taken to be 196 GHz in an 8 GHz bandwidth [8].

The specific effective surface area $\sigma_0(f,\psi)$ of a land cover comes from the following approximate empirical expression in the case of coherent horizontal polarization [15]

$$\sigma_0(f,\psi)=Z_1+Z_2\log(\psi/20)+Z_3\log(f/10), \quad (21)$$

where f is the central frequency in GHz (196 GHz), ψ is the grazing angle (the coverage sector $\theta_s(S,T,B_i,B_e)$ of the NRS antenna system), Z_1, Z_2, and Z_3 are the soil parameters for mapping various land covers. They are – 49, 32, and 20 dB for concrete and – 21, 10, and 6 dB for grass [15].

We obtained $\sigma_0(196,70)\sim -4$ dB for concrete and $\sigma_0(196,70)\sim -1$ dB for grass. Yet, at 10, 15 GHz, and 37.5 GHz frequencies, the $\sigma_0(f,\psi)$ values do not align closely with the experimental results [15]. The variations are approximately between 0.8 and 3.8 dB.

13. Transmitter pulse power P_t for mapping surface backlighting [2, 14]. Of concern are the repetition period T_r and duration τ_i of pulsed noise-like probing signals for backlighting. If decoupling between transmitter signals and BR receivers is not possible, quasi-continuous radiation is recommended. For backlighting, a meander-shaped noise-like signal with a repetition period T_r that is twice the duration τ_i of the pulsed probing signal is adopted,

$$\tau_i=$$
$$=2\sqrt{R_2(S,T,B_i,B_e)^2-[0.5B_{im}(S,T,B_i,B_e)]^2}\big/c, \quad (22)$$

where c is the speed of light ($3\cdot 10^8$ m/s).

We found that $\tau_i\le 6$ μs and $T_r\sim 12$ μs. With the F_{pij} measured, $\tau_i\le 4$ μs and $T_r\sim 8$ μs.

The number of accumulated echo signals is

$$M(S,T,B_i,B_e,\tau_i)=\frac{\sqrt{2}\,\alpha_1 t_p(S,T,B_i,B_e)\Theta_3}{4\tau_i\theta_s(S,T,B_i,B_e)}, \quad (23)$$

where α_1 is the proportionality coefficient. For a rectangular wave packet accumulating all the pulses, $\alpha_1=1$. Ibidem, $\Theta_3=(\sqrt{2}\,\lambda_3 180)/(\pi L_1)$, where $\lambda_3=1.53$ mm, is the half-width of the radiation pat-

tern of the transmitter antenna and the antennas of the BR receiving channels (degrees).

We obtained $M(10^2,275,10^3,10^3,6\cdot10^{-6})\sim 253$ echo-signals. During F_{pij} measuring, we obtained $M(10^2,275,10^3,20,4\cdot10^{-6})\sim 421$ echo-signals.

The absolute noise temperature T_a of the BR antennas is

$$T_a=(1-\beta)\eta\times$$
$$\times\left[T_{at}+t_{g2}C_2(1-\delta)+\sum_{i=1}^{n}t_iC_2\delta_i+TC_2\delta\right]+$$
$$+\beta\eta\left(T_{at}+t_{g2}C_2+\sum_{j=1}^{k}t_jC_2\delta_j\right)+(1-\eta)T_0, \qquad (24)$$

where β is the antenna dispersion coefficient, η is the antenna efficiency, T_{at}, t_{g2}, T, T_0 are the noise (radio-brightness) temperatures of the atmosphere, ground, and the object, respectively, and T_0 is the absolute temperature of the environment. Ibidem, $C_2\sim 0.563$ (see expression (7)), t_i, t_j, $i=1,2,\dots n$ and $j=1,2,\dots k$ are the noise temperatures of surfaces that interfere with the reception of useful signals in, respectively, the main and side lobes of the radiation patterns of the antennas, δ is the relation between the solid angles occupied by the object and by the main lobe of the BR antenna radiation pattern, and δ_i and δ_j are the same as δ but for signals interfering with the reception of object vibrations.

We adopted $\beta=0.31$, $\eta=0.78$, $t_{g2}=292$ K, $\delta=0.2(0.5)$, $T=274$ K, and $T_0=290$ K. Then $T_a\sim$ ~ 290 K if the Doppler frequency correction F_{pij} is not measured. If measured, $T_a\sim 288$ K.

Let us determine the noise figure K_n of the BR receiving channels, which process echo-signals from the surfaces under backlighting [14, 17]. The structure circuitry features a classic series connection of a circulator, a low-noise G-band amplifier, a preselector, a mixer, an amplifier, and a band-pass filter. For a low-noise amplifier with a noise figure of 7 dB at a gain of 20 dB [20], we obtained $K_n\sim 5.3$.

The noise spectral density $N_0(T_a)$ in the BR receiving channels, the opening area A_a of the antennas, and the radar cross-section (RCS) $\sigma_t(\sigma_0,S)$ of mapped objects are obtained by the formulas [14, 16]

$$N_0(T_a)=kT_0\left[K_n-1+(T_a/T_0)\right],$$
$$A_a\sim 0.4\pi(0.5D^2), \qquad (25)$$
$$\sigma_t(\sigma_0,S)=10^{(-\sigma_0/10)}S,$$

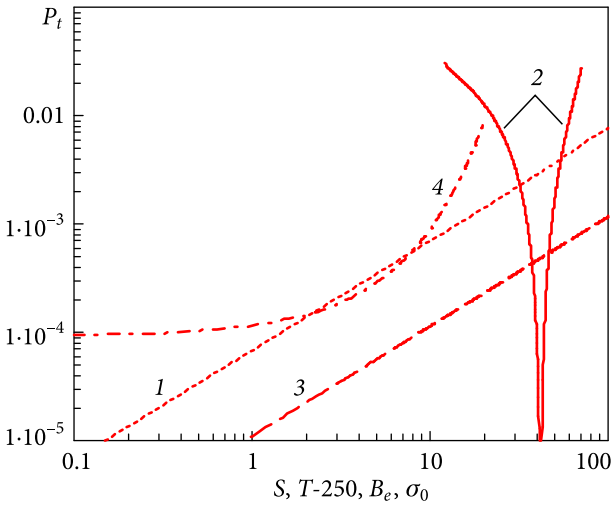

Fig. 7. Powers $P_t(S,T,B_i,B_e,T_a,\sigma_0)$ of the pulse transmitter of the noise-like quasi-continuous signal for mapping surface "backlighting" depending on variables S, T, B_e, and σ_0: *1* — $P_t(S,274,10^3,10^3,290,4)$; *2* — $P_t(10^2,T,10^3,10^3,290,4)$; *3* — $P_t(10^2,274,10^3,B_e,288,4)$; *4* — $P_t(10^2,274,10^3,20,288,\sigma_0)$

where k is the Boltzmann constant ($1.38\cdot10^{-23}$ J/K) and σ_0 is the specific radar cross-section (RCS) of a ground cover. Using formula (21), we have $\sigma_0\sim -4$ dB for concrete and for grass, $\sigma_0\sim -1$ dB. We obtained $N_0(288)=2.12\cdot10^{-20}$ J, $A_a\sim 7.22\cdot10^{-3}$ m^2 and $\sigma_t(4,10^2)\sim 39.8$ m^2.

The pulse transmitter power $P_t(S,T,B_i,B_e,T_a,\sigma_0)$ of the noise-like quasi-continuous signal for the mapping surface backlighting comes from the formula [14–18]

$$P_t(S,T,B_i,B_e,T_a,\sigma_0)=$$
$$=\frac{2\pi^2\nu_1N_0(T_a)\theta_s(S,T,B_i,B_e)R_2(S,T,B_i,B_e)^4L_l}{45t_p(S,T,B_i,B_e)A_a\sigma_n(\sigma_0,S)}, \qquad (26)$$

where L_l is the loss for the echo-signal reception and processing, it is assigned to be 10 dB.

The calculation results of the backlighting pulse transmitter power are presented in Fig. 7. The dependences $P_t(S,274,10^3,10^3,290,4)$ (straight line *1*) and $P_t(10^2,T,10^3,10^3,290,4)$ (curve *2*) indicate the transmitter power values with the correction F_{pij} not measured. For clarity, curve *2* is shifted by 250 K. The dependences $P_t(10^2,274,10^3,B_e,288,4)$ (straight line *3*) and $P_t(10^2,274,10^3,10^3,288,\sigma_0)$ (curve *4*) describe the backlighting powers with the F_{pij} correction measured. Additionally, possible changes in the Doppler filter band B_e and the specific RCS σ_0 of the mapping surfaces are shown.

To sum up, when $B_i = B_e = 10^3$ Hz, $R_{2ij} \sim 2.95$ km, $B_{imij} \sim 4.53$ km, $n_{kij} \sim 1106$ and $M_{ij} \sim 250$, and $\theta_{sij} \sim \pm 50.1°$, then $P_t(10^2, 274, 10^3, 10^3, 290, 4) \sim$ ~ 7.7 mW. With the F_{pij} measured ($B_3 = 10^3$ Hz and $B_e = 20$ Hz), we have, correspondingly, $R_{2ij} \sim$ ~ 1.28 km, $B_{imij} \sim 0.82$ km, $n_{kij} \sim 472$, $M_{ij} \sim 420$, and $P_t(10^2, 274, 10^3, 20, 288, 4) \sim 0.23$ mW. Such a drop in the backlighting power in the F_{pij} presence is associated with a decrease in the BR values B_{imij} and R_{2ij}.

14. Differential Doppler frequency correction $F_i(\vec{V}_o, \eta, S, T, B_i, B_e)$ under condition of ground backlighting [19, 20]. It is quite difficult to correlate the differential Doppler frequency correction F_{pij} of radiometric signals with the total Doppler frequency correction F_{iij} under backlighting conditions. In this connection, the F_{iij} and F_{pij} measurement algorithms are held the same, i.e., in the two BR receiving channels at $\lambda_3 = 1.53$ mm,

$$F_i(\vec{V}_o, \eta, S, T, B_i, B_e) = \\ = \left[\lambda_2 F_p(\vec{V}_o, \eta, S, T, B_i, B_e) \right] / \lambda_3 . \quad (27)$$

Due to the selected λ_3, F_{iij} decreases against F_{pij} slightly, by a factor of ~ 1.142. If F_{iij} is ~ 4.2 m/s, then F_{pij} is ~ 5.2 m/s.

The F_{iij} curves behave the same as the F_{pij} curves in Fig. 5.

Notably, when the bandwidth of the input low-noise amplifier is sufficiently wide to encompass the passive reception and backlighting ranges 192 to 232 GHz, no additional specialized echo-processing equipment is required. The output cross-correlation functions of the radiometric and backlighting channels differ by the frequency $1/T_r$. In the considered structure embodiment, this difference $1/T_r$ is approximately 125 kHz.

15. Root mean square (RMS) deviations of potential accuracies of delay time and differential Doppler frequency correction measurements [14]. The RMS deviations $\sigma_\tau(B, \nu)$ of the potential accuracy of the delay time measurements and the RMS deviations $\sigma_F(B_e, \nu)$ of the BR potential accuracy of the differential Doppler frequency correction measurements are evaluated by the formulas [14]

$$\sigma_{\tau 2}(B_p, \nu) = \sqrt{3}\, c / (\pi \nu B_p), \\ \sigma_{\tau 3}(B_b, \nu) = \sqrt{3}\, c / (\pi \nu B_b), \quad (28) \\ \sigma_F(B_e, \nu) = \sqrt{3}\, B_e / (\pi \nu),$$

where ν is the voltage SNR in land surface mapping and B_p is the BR input bandwidth. In the passive reception channel, $B_p = 14.5 \cdot 10^9$ Hz. Under backlighting, $B_p = B_b = 8 \cdot 10^9$ Hz.

For regular measuring, $\nu^2 >> 1$ is necessary. That is, the voltage SNR must be elevated from ~ 2.16 (previously adopted in our modeling) to no less than 32. We obtained $\sigma_{\tau 2}(14.5 \cdot 10^9, 32) \sim 0.36$ mm, $\sigma_{\tau 3}(8 \cdot 10^9, 32) \sim 0.64$ mm, and $\sigma_F(20, 32) \sim 0.35$ Hz. Such a high SNR can be achieved, e.g., by cooling the input circuits of the BR receiving channels, or by reducing the range R_{2ij} and the surface imagery band B_{imij}.

It is worth noting that the BR implementation in the infrared (3.3 to 4.2 μm) provides certain advantages in the resolution (P_{rij}) by path difference on the mapping surface [22]. Let us reduce the base B from 10 to 1 m. Then at $R_{2ij} \sim 2.95$ km, the resolution is $P_{rij} \sim 0.09$ m if in the infrared. In the 1 mm band, $P_{rij} \sim 12.2$ m. With F_{pij} correction measured, we had $R_{2ij} \sim 1.26$ km and $P_{rij} \sim 5.2$ m. Compare it with $P_{rij} \sim 0.04$ m in the infrared at the same $R_{2ij} \sim$ ~ 1.26 km range. The differential Doppler frequency correction F_{pij} in the infrared increases by approximately 357 times against the same BR construction in the 1 mm wave band.

Conclusions

A numerical model for determining the characteristics and parameters of the noise radar sensor (NRS) used for land cover mapping has been developed. The model utilizes radiometric signals from surfaces as well as echo signals from the same surfaces when illuminated with ultra-weak power noise signals.

Based on the adopted and technologically feasible NRS characteristics, high-quality mapping of land covers relying on their radiometric signals has been demonstrated. The BR range R_{1ij} with the central wavelength $\lambda_1 = 3.37$ mm and a 6.0 GHz band was compared to the BR range R_{2ij} with $\lambda_2 = 1.34$ mm and a 14.5 GHz band. The comparison indicates that the utility of a 1.34 mm radiometric signal is most evident in the BR. The BR provides the target detection by angles and path differences. In this case, the radiation patterns of the BR antennas contain six elements of discrimination by path difference on the ground, the radiometric image fluctuation sensitivity being $T_{fluct} = 0.41$ K.

Let, for instance, the BR output filter bandpass be $B_i = 10^3$ Hz, and let the Doppler filter bandpass be the same, $B_e = 10^3$ Hz. Then the BR range is $R_{2ij} \sim$ ~ 2.95 km with the image band $B_{imij} \sim 4.53$ km. The resolutions in and across the flight track are, respectively, $P_{ryij} \sim 12$ m and $P_{rxij} \sim 37$ m. The number of steps in one image line is $n_{kij} \sim 1106$, and the number of pixels in one line is $n_{pix.ij} \sim 6678$. The coverage sector of the BR antennas is $\theta_{sij} \sim \pm 50.1°$.

A method has been proposed for determining the wind velocity on the mapping surface. Narrow-band filters B_i of the differential Doppler frequency correction are installed at the exit of the BR output filter B_e. The useful signal accumulation time is limited and set at a $3/B_i$ level. For example, when $B_i = 10^3$ Hz and $B_e = 20$ Hz, then the SNR loss $\Delta = 14.8$ dB. Additionally, $R_{2ij} \sim 1.26$ km, $B_{imij} \sim 0.82$ km, $P_{ryij} \sim 5$ m, $P_{rxij} \sim 16$ m, $n_{kij} \sim 472$, $n_{pix.ij} \sim 2847$, $\theta_{sij} \sim \pm 19.1°$, the wind velocity resolution is $P_{rV_w} \sim$ ~ 4.5 m/s, and the number of Doppler filters is $N_{fij} = 7$ (at $V_w = 30$ m/s). The RMS deviation of the delay time potential measurement accuracy is $\sigma_{\tau 2ij} >> 5$ mm, and the RMS deviation of the potential measurement accuracy of differential Doppler frequency correction is $\sigma_{Fij} >> 5$ Hz.

Regular measuring the path differences and differential Doppler frequency corrections F_{pij} of useful signals is possible, provided that the voltage SNR at the BR output is approximately 8 rather than ~ 2.2. The SNR enhancement for $B_i = 10^3$ Hz, $B_e = 20$ Hz, and $\Delta \sim 14.8$ dB provided: $R_{2ij} \sim 0.65$ km, $B_{imij} \sim$ ~ 0.22 km, $P_{ryij} \sim 2.7$ m, $P_{rxij} \sim 8$ m, $n_{kij} \sim 244$, $n_{pix.ij} \sim$ ~ 1475, $\theta_{sij} \sim \pm 9.8°$, $P_{rV_w} \sim 2.2$ m/s, $N_{fij} = 14$ (at $V_w = 30$ m/s), $\sigma_{\tau 2ij} \sim 0.36$ mm, and $\sigma_{Fij} \sim 0.35$ Hz.

The cooling of the BR input circuits to depress the noise figures from approximately 6.7 to 2 significantly improves the NRS characteristics and parameters. For $B_i = 10^3$ Hz, $B_e = 20$ Hz, $\Delta \sim 14.8$ dB, we had $R_{2ij} \sim 1.13$ km, $B_{imij} \sim 0.67$ km, $P_{ryij} \sim 4.7$ m, $P_{rxij} \sim$ ~ 14 m, $n_{kij} \sim 424$, $n_{pix.ij} \sim 2559$, $\theta_{sij} \sim \pm 17.1°$, $P_{rV_w} \sim$ ~ 4 m/s, $N_{fij} = 8$ (at $V_w = 30$ m/s), $\sigma_{\tau 2ij} \sim 0.36$ mm, and $\sigma_{Fij} \sim 0.35$ Hz.

The Earth's surface probing with an ultra-weak-power noise signal enhances the imagery analysis. For decoupling the NRS receiving channels and the transmitter, echo signal detections and F_{pij} measurements are proposed to be performed under quasi-continuous radiation of the transmitter. Using an approximate empirical expression, we found specific effective scattering surfaces of concrete and grass at the transmitter wavelength $\lambda_3 = 1.53$ mm. The relevant power P_{tij} of the pulse noise transmitter was found along with pulse duration τ_{iij} and period T_{rij}. Specifically, we had $\tau_{iij} = 6$ μs, $T_{rij} = 12$ μs, and $P_{tij} \sim$ ~ 7.7 mW for $R_{2ij} \sim 2.95$ km. And $\tau_{iij} = 4$ μs, $T_{rij} =$ = 8 μs, and $P_{tij} \sim 0.23$ mW for $R_{2ij} \sim 2.95$ km. To prevent difficulties in identifying Doppler frequency corrections F_{pij} in the radiometric and backlighting channels, the measurements were conducted in the same manner as in the echo signal processing. The ratio between the differential Doppler frequencies in the radiometric and backlighting channels was approximately 1.14.

The main NRS characteristics and parameters in radiometric mode and under conditions of land cover backlighting have been optimized. The utility of the land cover mapping is most apparent in the transparency window 3.3 to 4.2 μm in the infrared.

REFERENCES

1. Sokolov, A.V. ed., 2003. *Issues of advanced radar*. Collective monograph. M.: Radio Engineering Publ.
2. Dulevich, V.E. ed., 1978. *Theoretical foundations of radiolocation.* 2nd ed. revised and enlarged. M.: Sov. Radio Publ.
3. Karavaev, V.V., Sazonov, V.V., 1987. *Statistical theory of passive radiolocation systems*. M.: Radio and Communication Publ.
4. Shilo, S.A., Sidorenko, Yu.B., 2009. *Method for forming radiometric images and antennas for its implementation.* Ukraine. Pat. 85932 (in Ukrainian).
5. Owda, A., Salmon, N., Rezqui, N., Shylo, S., 2017. Millimetre Wave Radiometers for Medical Diagnostics of Human Skin. In: *2017 IEEE Sensors*: proc. Glasgow, UK, 29 Oct. — 1 Nov. 2017, pp. 768—770. IEEE. DOI: 10.1109/ICSENS.2017.8234132
6. Kudryashov, V.E., 2018. A Bistatic Radiometry System for Object Mapping, Telecommunicati ons and Radio Engineering. *Telecommunications and Radio Engineering*, **77**(20), pp. 1813—1826. DOI: 10.1615/TelecomRadEng.v77.i20.40
7. Kudryashov, V.E., Litovchenko, D.M., Filippenkov, O.V., 2020. Multi-channel reception system for radiometry signals. In: *2020 IEEE Ukrainian Microwave Week (UkrMW)*: proc. Kharkiv, Ukraine, 21—23 Sept. 2020, pp. 318—322. IEEE. DOI: 10.1109/UkrMW49653.2020.9252699
8. *Radio Regulations*. Articles. Geneva: Switzerland, 2016. 441 p.

9. Kudriashov, V., Garbar, A.Y., Lukin, K.A., Maslikowski, L., Samczynski, P., Kulpa, K., 2015. Fusion of Images Generated by Radiometric and Active Noise SAR. *Cybern. Inf. Technol*., **15**(7), pp. 58—66. DOI: 10.1515/cait-2015-0089
10. Lukin, K.A., & Kudriashov, V.V., 2013. Fusion of synthetic aperture radiometer and noise waveform SAR images. In: *2013 IX Int. Conf. Antenna Theory and Techniques (ICATT)*: proc. Odessa, Ukraine, 16—20 Sept. 2013, pp. 549—551. IEEE. DOI: 10.1109/ICATT.2013.6650843
11. Kudriashov, V., 2015. A modified maximum likelihood method for estimation of mutual delay and power of noise signals by bistatic radiometer. *Comptes rendus de l'Académie bulgare des Sciences*, **68**(5), pp. 631—640.
12. Skolnik, M. ed., 1978. *Handbook of Radiolocation*. Vol. 4. Radar Stations and Systems. M.: Sov. Radio Publ.
13. Tikhonov, V.I. ed., 1980. *Statistical Radio Engineering: Examples and Problems*. M.: Sov. Radio Publ.
14. Shirman, Ya.D. ed., 1970. *Theoretical Foundations of Radiolocation*. M.: Sov. Radio Publ.
15. Shirman, Ya.D. ed., 2007. *Radioelectronic Systems: Basics of Design and Theory. Handbook*. 2nd revised and enlarged ed. M.: Radio Engineering Publ.
16. Skolnik, M. ed., 1976. *Handbook of Radiolocation*. Vol. 1. Fundamentals of Radiolocation. M.: Sov. Radio Publ.
17. *Eravant. Low Noise Amplifiers*. Available from: https://www.eravant.com/products/amplifiers/low-noise-amplifiers
18. Bronstein, I.N., Semendyaev, K.A., 1981. *Handbook of Mathematics for Engineers and University Students*. M.: Science Publ.
19. Almazov, V.B., 1974. *Methods of Passive Radar*. Kharkiv: VIRTA Publ.
20. Chernyak, V.S., 1993. *Multi-position radiolocation*. M.: Radio and Communication Publ.
21. Kudriashov, V., Martin-Neira, M., Roelofs, F., Falcke, H., Brinkerink, C., Baryshev, A., Hogerheijde, M., Young, A., Pourshaghaghi, H., Klein-Wolt, M., Moscibrodzka, M., Davelaar, J., Barat, I., Duesmann, B., Valenta, V., Perdigues Armengol, J.M., De Wilde, D., Martin Iglesias, P., Alagha, N., Van Der Vorst, M., 2021. An Event Horizon Imager (EHI) Mission Concept Utilizing Medium Earth Orbit Sub-Mm Interferometry. *Chinese Journal of Space Science (CJSS)*, **41**(2), pp. 211—233. DOI: 10.11728/cjss2021.02.211
22. Skolnik, M.I., 1981. *Introduction to Radar Systems*. Second Ed. Singapore: McGraw-Hill Book Co.

Received 11.01.2025

В.Є. Кудряшов, К.О. Лукін, Д.М. Татьянко

Інститут радіофізики та електроніки ім. О.Я. Усикова НАН України
вул. Акад. Проскури, 12, м. Харків, 61085, Україна

ЧИСЛОВЕ МОДЕЛЮВАННЯ ХАРАКТЕРИСТИК
І ПАРАМЕТРІВ ШУМОВОГО РАДАРНОГО СЕНСОРА
ДЛЯ КАРТОГРАФУВАННЯ ЗЕМНОЇ ПОВЕРХНІ

Предмет і мета роботи. У роботі наведено результати числового моделювання характеристик і параметрів шумового радарного сенсора (ШРС) при дистанційному зондуванні земних поверхонь. Розглянуто радіометричний (пасивний) режим роботи і режим з «підсвічуванням» (активний) сцен картографування. Застосовано радіометричні сигнали поверхонь на довжинах хвиль 3.37 і 1.34 мм та ехо-сигнали за умов «підсвічування» цих же поверхонь шумовим квазінеперервним сигналом надслабкої потужності з $\lambda = 1.53$ мм. Мета роботи полягає у розробленні методики числового моделювання для розрахунку можливих вхідних характеристик ШРС та їх порівняння з вихідними параметрами зображень об'єктів картографування.

Методи та методологія. Проведено аналіз і синтез отриманих вихідних параметрів та характеристик зображень земних поверхонь за можливими варіантами побудови ШРС. Як носій ШРС запропоновано використовувати літак АН-14 «Бджілка». Ураховувалися стан атмосфери та обмежений час накопичення малоконтрастного радіометричного корисного сигналу «трава–бетон». Визначено приблизні питомі ефективні поверхні розсіювання трави та бетону в режимі «підсвічування».

Результати. Виконано оптимізацію результатів числового моделювання характеристик і параметрів ШРС у двох режимах роботи. Отримані такі значення параметрів системи: дальність дії в радіометричному режимі та за умов «підсвічування» цих же поверхонь; сектор огляду поверхонь і смуги зображення; роздільна здатність; кількість доплерівських фільтрів на виходах ШРС; точнісні характеристики системи.

Висновки. Числове моделювання виконано для характеристик ШРС, які технічно реалізуються на практиці. Проведено оптимізацію основних параметрів ШРС у радіометричному режимі роботи та при «підсвічуванні» сцен картографування. Визначено залежності між вхідними характеристиками ШРС з вихідними параметрами зображень земних поверхонь. Отримані результати дозволять прогнозувати якість зображень при дистанційному зондуванні.

Ключові слова: *радіометричний контраст, трава, бетон, дальність дії, піксель, доплерівська поправка частоти, роздільна здатність, середньоквадратичне відхилення помилок.*